

Statistically study the optimal local sources for cosmic ray nuclei and electron

QING LUO,^{1,2} BING-QIANG QIAO,² WEI LIU,² SHU-WANG CUI,¹ AND YI-QING GUO^{2,3}

¹ *Hebei Normal University, Shijiazhuang 050024, Hebei, China*

² *Key Laboratory of Particle Astrophysics, Institute of High Energy Physics, Chinese Academy of Sciences, Beijing 100049, China*

³ *University of Chinese Academy of Sciences, Beijing 100049, China*

ABSTRACT

The local sources, such as Geminga SNR, may play important role for the anomaly of proton, electron and anisotropy in the past works. In fact, there exists twelve SNRs around solar system within 1 kpc. One question is that can other SNRs also possibly contribute the spectra of nuclei and electron and explain the special structure of anisotropy? In this work, under the spatial-dependent propagation, we systematically study the contribution of all local SNRs within 1 kpc around solar to the spectra of nuclei and electron, as well as the energy dependence of anisotropy. As a result, only Geminga, Monogem, and Vela SNRs have quantitative contribution to the nuclei and electron spectra and anisotropy. Here, Geminga SNR is the sole optimal candidate and Monogem SNR is controversial due to the tension of anisotropy between model calculation and observations. The Vela SNR contributes a new spectral structure beyond TeV energy, hinted by HESS, VERITAS, DAMPE and CALET measurements. More interesting is that the electron anisotropy satisfies the Fermi-LAT limit below TeV energy, but rises greatly and reaches 10% at several TeV. This new structure will shed new light to check our model. We hope that the new structure of electron spectrum and anisotropy can be observed by space-borne DAMPE and HERD and ground-based HAWC and LHAASO experiments in the near future.

1. INTRODUCTION

It is well known that supernova remnants (SNRs) are the dominant source of galactic cosmic rays (GCRs) (Boulares 1989; Blasi 2013; Ackermann et al. 2013). In this scenario, the expanding diffusive shocks accelerate cosmic rays (CRs) to very high energy (VHE). The electron and nuclei are concomitant and can both be accelerated to VHE simultaneously. This means that the nuclei and electron have common origin (Yuan & Bi 2013). The combined study for such multi-messenger topic is very important to unveil the enigma of CRs origin. The typical properties of observations are required to support this view of point.

The measurements of CRs are stepping into an era of high precision with new generation of space-borne and ground-based experiments. A series of new phenomena are revealed with those new precise measurements. Firstly, a fine structure of spectral hardening at 200 GV for nuclei were discovered by ATIC-2, CREAM and PAMELA experiments (Panov et al. 2007, 2009;

Ahn et al. 2010; Yoon et al. 2017; Adriani et al. 2011). Lately, AMS-02 experiment confirmed it with unprecedented precision (Aguilar et al. 2015b,a). More interesting is that the spectral break-off around \sim 14 TeV was observed by CREAM, NUCLEON and DAMPE experiments (Yoon et al. 2017; Atkin et al. 2017, 2018; An et al. 2019; Alemanno et al. 2021). Three categories of models as the local source (Sveshnikova et al. 2013; Liu et al. 2017, 2019; Vladimirov et al. 2012), the combined effects from different group sources (Malkov & Moskalenko 2020) and the spatial-dependent propagation (SDP) (Guo et al. 2016; Jin et al. 2016; Guo & Yuan 2018; Liu et al. 2018) are proposed to explain these new structure. Similar to the nuclei, the electron should exist such component above \sim 100 GeV. The recent precise spectrum measurement shows sharp dropoff at 284 GeV for positron but without obvious change until TeV for the total spectrum of electron and positron. The deficit of positron above 284 GeV required the compensation of primary electron. This means that the electron excess exists similar to the fine structure of nuclei, which is possibly accelerated in the SNRs scenario (Mertsch 2011; Bernard et al. 2012; Serpico 2012; Di Mauro et al. 2014; Fang et al. 2018b; Tang & Piran 2019).

More important is the anisotropy evolution with energy. Though the arrival directions of GCRs are highly

Corresponding author: Bing-qiang Qiao, Wei Liu, Shu-wang Cui, Yi-qing Guo
 qiaobq@ihep.ac.cn, liuwei@ihep.ac.cn, cuiws@hebtu.edu.cn,
 guoyq@ihep.ac.cn

isotropic due to their diffusive propagation in the Galactic magnetic field, a weak dipole-like anisotropy is consistently observed, with intensity differences up to $\sim 10^{-4} - 10^{-3}$. So far a large amount of observations of anisotropies ranging from TeV to PeV have been carried out by the ground-based experiments, for example Super-Kamiokande Guillian et al. (2007), Tibet Amenomori et al. (2005, 2006, 2010, 2017), Milagro Abdo et al. (2008, 2009), IceCube/Ice-Top Abbasi et al. (2010, 2011, 2012); Aartsen et al. (2013, 2016), ARGO-YBJ Bartoli et al. (2013, 2015) and HAWC Abeysekara et al. (2014). It is clear that the phase of anisotropy below 100 TeV roughly directs to galactic anticenter, which is totally paradoxical with the conventional propagation model (CPM). However, above 100 TeV, the phase directs to galactic center and is consistent with the expectation of CPM. Correspondingly, the amplitude has experienced similar transition at the critical energy of 100 TeV. In addition, the most importance is that there exists a common transition energy scale between the structures of the energy spectra and the anisotropy. The local source possibly plays very important role to resolve the conjunct problems of spectra and anisotropy (Liu et al. 2019; Qiao et al. 2019).

Based on the above discussion, the local source is required to reproduce the multi-messenger anomaly for spectra of proton and electron and nuclear anisotropy. In our recent work, we propose a local source under the SDP model to reproduce the co-evolution of the spectra and anisotropy. We find that the Geminga SNR at its birth place could be a preferred candidate (Liu et al. 2019; Qiao et al. 2019; Zhang et al. 2021). One natural question is that there are dozens of SNRs near solar within 1 kpc as shown in Figure 1, how about the contribution from other SNRs? In this work, we will systematically study the contribution of all local SNRs within 1 kpc around solar to the spectra of nuclei and electron, the detailed parameters of these local SNRs are shown in Table 1. The paper is organized as follows. Section 2 gives model description, Section 3 presents the calculated results and Section 4 describes the conclusion.

2. MODEL DESCRIPTION

After entering the interstellar space, CRs undergo the random walks within the Galactic magnetic field by bouncing off the magnetic waves and magnetohydrodynamic turbulence. The diffusive region, which is called magnetic halo, is approximated as a flat cylinder with its radius $R = 20$ kpc, equivalent to the Galactic radius. The half-thickness z_h is unknown, and is typically constrained by fitting the B/C ratio. The Galactic disk, where both cosmic ray (CR) sources and interstellar gas

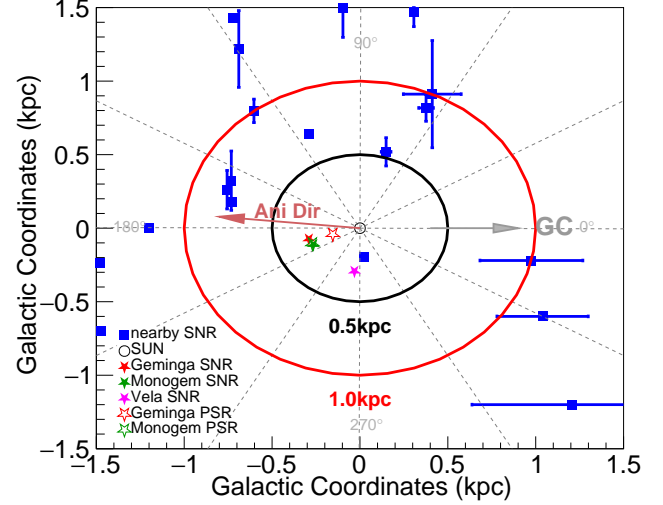


Fig. 1. Face-on view of the galaxy showing positions of the local SNRs within 1 kpc from the solar system. The blue solid squares mark the SNRs. The hollow circle represent the location of the solar system. The solid red, green and pink pentagrams represent Geminga, Monogem, and Vela SNR respectively and the hollow ones represent homologous pulsar. The gray arrow points to the galactic center and the brown arrow indicates the direction of CRs anisotropy below ~ 100 TeV.

are mainly spread across, is located in the middle of the magnetic halo. The width of Galactic disk is approximated to be invariant spatially and equals to 200 pc. In addition to diffusion, CRs may still go through convection, diffusive-reacceleration, fragmentation, radioactive decay and other energy losses before arriving at the solar system. In fact, the processes of convection is ignored in this work. CR nuclei lose their energy principally via ionization, Coulomb scattering and adiabatic expansion. For electrons and positrons, their major energy losses are the bremsstrahlung, synchrotron radiation and the inverse Compton scattering. This comprehensive process can be described by the propagation equation as:

$$\begin{aligned} \frac{\partial \psi(\mathbf{r}, p, t)}{\partial t} &= q(\mathbf{r}, p, t) + \nabla \cdot (D_{xx} \nabla \psi - \mathbf{V}_c \psi) \\ &+ \frac{\partial}{\partial p} p^2 D_{pp} \frac{\partial}{\partial p} \frac{1}{p^2} \psi - \frac{\partial}{\partial p} [\dot{p} \psi - \frac{p}{3} (\nabla \cdot \mathbf{V}_c \psi)] \\ &- \frac{\psi}{\tau_f} - \frac{\psi}{\tau_r} \end{aligned} \quad (1)$$

where $q(\mathbf{r}, p, t)$ is the acceleration sources, $\psi(\mathbf{r}, p, t)$ is the density of CR particles per unit momentum p at position \mathbf{r} , \mathbf{V}_c is the convection velocity, $\dot{p} \equiv dp/dt$ is momentum loss rate, τ_f and τ_r are the characteristic time scales for fragmentation and radioactive decay respectively; D_{xx} and D_{pp} are the diffusion coefficients in coordinate and momentum space respectively.

Number	SNR G+long+lat	Other name	Distance [kpc]	Radio index α_r	Age [kyr]	Pulsar	References
1	G194.3-13.1	Geminga	0.33		345	J0633+1746	(1)
2	65.3+5.7		0.9 ± 0.1	0.58 ± 0.07	26 ± 1		(2-5)
3	65.7+1.2	DA 495	1.0 ± 0.4	0.45 ± 0.1	16.75 ± 3.25	unkown	(6,7)
4	74.0-8.5	Cygnus Loop	$0.54^{+0.10}_{-0.08}$	0.4 ± 0.06	10 ± 1	J1952+3252	(5,8,9)
5	114.3+0.3		0.7	0.49 ± 0.25	7.7 ± 0.1		(5,6,10,11)
6	127.1+0.5	R5	1 ± 0.1	0.43 ± 0.1	25 ± 5		(5,6,11-13)
7	156.2+5.7		0.8 ± 0.5	$2.0^{+1.1}_{-0.7}$	10 ± 1	B0450+55	(5,6,14-17)
8	160.9+2.6	HB 9	0.8 ± 0.4	0.48 ± 0.03	5.5 ± 1.5	B0458+46	(5,6,11,18,19)
9	203.0+12.0	Monogem Ring	$0.288^{+0.033}_{-0.027}$		86 ± 1	B0656+14	(20-21)
10	263.9-3.3	Vela(XYZ)	0.295 ± 0.075	variable	11.2 ± 0.1	B0833-45	(5,22-25)
11	266.2-1.2	Vela Jr	0.75 ± 0.01		3.5 ± 0.8	J0855-4644	(5,26-29)
12	347.3-0.5	SN393	1 ± 0.3		4.9		(5,30-31)

1([Smith et al. 1994](#));2([Gorham et al. 1996](#));3([Mavromatakis et al. 2002](#));4([Xiao et al. 2009](#));5([Green 2014](#));6([Kothes et al. 2006](#));7([Kothes et al. 2008](#));8([Blair et al. 2005](#));9([Sun et al. 2006](#));10([Yar-Uyaniker et al. 2004](#));11([Reich et al. 2014](#));12([Joncas et al. 1989](#));13([Leahy & Tian 2006](#));14([Reich et al. 1992](#));15([Yamauchi et al. 2000](#));16([Xu et al. 2007](#));17([Katsuda et al. 2009](#));18([Reich et al. 2003](#));19([Leahy & Tian 2007](#));20([Plucinsky et al. 1996](#));21([Brisken et al. 2003](#));22([Cha et al. 1999](#));23([Alvarez et al. 2001](#));24([Caraveo et al. 2001](#));25([Miceli et al. 2008](#));26([Aschenbach 1998](#));27([Iyudin et al. 1998](#));28([Redman & Meaburn 2005](#));29([Katsuda et al. 2008](#));30([Lazendic et al. 2004](#));31([Morlino et al. 2009](#)).

Tab. 1. Characteristic parameters of nearby SNRs within 1 kpc.

2.1. Spatially-dependent propagation

The SDP of CRs has received a lot of attention in recent years. It was first introduced as a Two Halo model (THM) ([Tomassetti 2012](#)) to explain the spectral hardening of both proton and helium above 200 GeV ([Adriani et al. 2011](#)). Afterwards, it is further applied to secondary and heavier components ([Tomassetti 2015](#); [Feng et al. 2016](#); [Guo et al. 2016](#); [Liu et al. 2018](#); [Tian et al. 2020](#); [Yuan et al. 2020](#)), diffuse gamma-ray distribution ([Guo & Yuan 2018](#)) and large-scale anisotropy ([Liu et al. 2019](#); [Qiao et al. 2019](#)). For a comprehensive introduction, one can refer to [Guo et al. \(2016\)](#) and [Liu et al. \(2018\)](#).

In the SDP model, the whole diffusive halo is divided into two parts. The Galactic disk and its surrounding area are called the inner halo (IH) region, in which the diffusion coefficient is spatially-dependent and relevant to the radial distribution of background CR sources. The extensive diffusive region outside the IH is named as the outer halo (OH) region, where the diffusion is regarded as only rigidity dependent. The spatially-dependent diffusion coefficient D_{xx} is thus parameterized as:

$$D_{xx}(r, z, \mathcal{R}) = D_0 F(r, z) \beta^\eta \left(\frac{\mathcal{R}}{\mathcal{R}_0} \right)^{\delta(r, z)}, \quad (2)$$

where r and z are cylindrical coordinate, \mathcal{R} is the particle's rigidity, β is the particle's velocity in unit of light speed, D_0 and η are constants. For the parameteriza-

tion of $F(r, z)$ and $\delta(r, z)$, one can refer to ([Tian et al. 2020](#)). The total half-thickness of the propagation halo is z_h , and the half-thickness of the inner halo is ξz_h .

In this work, we adopt the common diffusion-reacceleration (DR) model, with the diffusive-reacceleration coefficient D_{pp} coupled to D_{xx} by $D_{pp} D_{xx} = \frac{4p^2 v_A^2}{3\delta(4 - \delta^2)(4 - \delta)}$, where v_A is the Alfvén velocity, p is the momentum, and δ is the rigidity dependence slope of the diffusion coefficient ([Seo & Ptuskin 1994](#)). The numerical package DRAGON is used to solve the SDP equation to obtain the distribution of CR positrons, electrons and protons. Less than tens of GeV, the CR fluxes are impacted by the solar modulation. The well-known force-field approximation ([Gleeson & Axford 1968](#); [Perko 1987](#)) is applied to describe such an effect, with a modulation potential ϕ adjusted to fit the low energy data.

2.2. Background sources

The SNRs are regarded as the most likely sites for the acceleration of GCRs by default, in which the charge particles are accelerated to a power-law distribution through the diffusive shock acceleration. The distribution of SNRs are approximated as axisymmetric, which is usually parameterized as

$$f(r, z) = \left(\frac{r}{r_\odot} \right)^\alpha \exp \left[-\frac{\beta(r - r_\odot)}{r_\odot} \right] \exp \left(-\frac{|z|}{z_s} \right), \quad (3)$$

where $r_\odot \equiv 8.5$ kpc represents the distance from solar to Galactic center. The parameters α and β are taken

as 1.69 and 3.33 respectively in this work (Green 2015). The density distribution of the SNRs decreases exponentially along the vertical height from the Galactic plane, with $z_s = 200$ pc.

The injection spectra of nuclei and electron are assumed to be exponentially cutoff broken power-law function of particle rigidity \mathcal{R} , i.e.

$$q(\mathcal{R}) = q_0 \begin{cases} \left(\frac{\mathcal{R}_{\text{br1}}}{\mathcal{R}_0}\right)^{\nu_2} \left(\frac{\mathcal{R}}{\mathcal{R}_{\text{br1}}}\right)^{\nu_1}, & \mathcal{R} \leq \mathcal{R}_{\text{br1}} \\ \left(\frac{\mathcal{R}}{\mathcal{R}_0}\right)^{\nu_2}, & \mathcal{R}_{\text{br1}} < \mathcal{R} \leq \mathcal{R}_{\text{br2}} \\ \left(\frac{\mathcal{R}_{\text{br2}}}{\mathcal{R}_0}\right)^{\nu_2} \left(\frac{\mathcal{R}}{\mathcal{R}_{\text{br2}}}\right)^{\nu_3} \exp\left[-\frac{\mathcal{R}}{\mathcal{R}_c}\right], & \mathcal{R} > \mathcal{R}_{\text{br2}} \end{cases} \quad (4)$$

where q_0 is the normalization factor, $\nu_{1,2,3}$ are the spectral incides, $\mathcal{R}_{\text{br1,2}}$ are break rigidities, \mathcal{R}_c is the cutoff rigidity, and \mathcal{R}_0 is a reference rigidity.

2.3. Local SNRs

At \sim TeV energies, CR electrons originate from local sources within ~ 1 kpc around the solar system (Yuan & Feng 2018). In this small region, the hypothesis of continuous distribution may not be valid any more. Studies show that the discrete effect of nearby CR sources could induce large fluctuations, especially at high energies (Mertsch 2011; Bernard et al. 2012; Fang et al. 2017). The contribution of nearby sources to CR nuclei and electrons have been studied in the past works(see e.g., (Serpico 2012; Di Mauro et al. 2014; Liu et al. 2017; Fang et al. 2018a)). In this work, we assume a nearby SNR to account for the electron(proton) excess above $\sim 100(200)$ GeV respectively. The propagation of CRs injected instantaneously from a point source is described by a time-dependent propagation equation (Atoyan et al. 1995). The injection rate as a function of time and rigidity is assumed to be

$$Q^{\text{snr}}(\mathcal{R}, t) = Q_0^{\text{snr}}(t) \left(\frac{\mathcal{R}}{\mathcal{R}_0}\right)^{-\gamma} \exp\left[-\frac{\mathcal{R}}{\mathcal{R}_c^{\text{e-},\text{p}}}\right], \quad (5)$$

where $\mathcal{R}_c^{\text{e-},\text{p}}$ is the cutoff rigidity of its accelerated CRs.

The local SNRs may accelerate primary nuclei and electrons during its early evolution stage. This contribution of primary electrons from local sources may be necessary, given the different spectral behaviors of positrons and electrons(Zhang et al. 2021). The injection process of the SNRs is approximated as burst-like. The source injection rate is assumed as following,

$$Q_0^{\text{snr}}(t) = q_0^{\text{snr}} \delta(t - t_0), \quad (6)$$

where t_0 is the time of the supernova explosion. The propagated spectrum from the local SNRs is thus a convolution of the Green's function and the time-dependent injection rate $Q_0(t)$ (Atoyan et al. 1995)

$$\varphi(\mathbf{r}, \mathcal{R}, t) = \int_{t_0}^t G(\mathbf{r} - \mathbf{r}', t - t', \mathcal{R}) Q_0(t') dt'. \quad (7)$$

3. RESULTS

The model parameters are tuned according to the B/C ratio, the energy spectra of CRs and the amplitudes of CRs anisotropies. The diffusion coefficient parameters are $D_0 = 4.87 \times 10^{28} \text{ cm}^2 \text{ s}^{-1}$, $\delta_0 = 0.55$, $N_m = 0.6$, $n = 4$, $\xi = 0.1$, and $\eta = 0.05$. The half thickness of the propagation halo is $z_h = 5$ kpc, and the Alfvénic velocity is $v_A = 6 \text{ km s}^{-1}$. The comparison of the B/C ratio between the model prediction and the data is given in Figure. 2, which indicates that the relevant parameters are reasonable. In order to determine which nearby SNRs are the appropriate candidates on the basis of their contributions for the proton and electron spectra respectively as following parts.

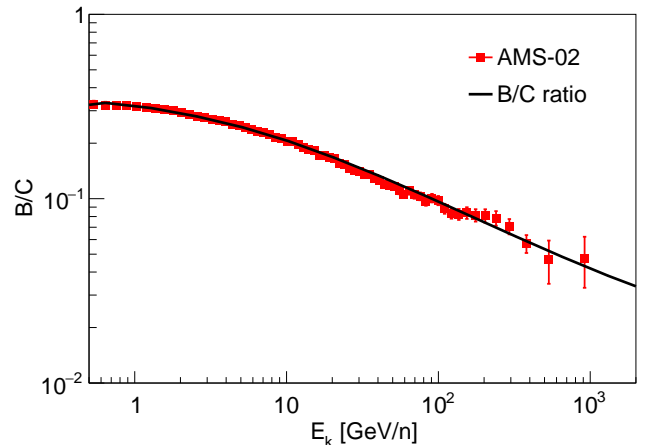


Fig. 2. Model prediction of the B/C ratio compared with AMS-02 measurement(Aguilar et al. 2015b, 2017).

3.1. Spectra of all the local SNRs

Figure 3 presents the calculated proton and electron spectra for all the SNRs listed in Table 1. Here it can be seen that only Geminga, Monogem and Vela SNRs have significant contributions to the proton and electron spectra respectively. Most of them have very limited contribution to the spectra. To appear in the same figure, we multiply a scale factor in the fluxes for the faint SNRs as shown the dashed line of Figure 3. The detailed parameters of local sources are listed in Table 2.

In the following subsection, we give the detailed studies on the contribution in the spectra and anisotropy for the Geminga, Monogem and Vela SNRs. By doing so, we can pinpoint the optimal local SNR.

3.2. Spectra and anisotropy of Geminga SNR

Figure 4 illustrates the calculated energy spectra and anisotropy of proton and primary electron respectively. The blue solid lines are the fluxes from the background sources. Taking into account the contributions of Geminga SNR as shown in Figure 3, the model predictions of proton and primary electron spectra are in good agreement with the experimental data as in the upper panel of Figure 4. Table 2 shows the relevant background and local source parameters. In fact, the anisotropy is more effective to determine the dominant local SNR from its direction, age and distance. The bottom panel of Figure 4 shows the model calculated anisotropy for CRs and electron respectively. It is obvious that the model calculations are consistent with observations for CRs. The electron one is roughly at the same level and far below the Fermi-LAT limit. Therefore the results support our previous conclusion of the co-evolution of spectrum and anisotropy for Geminga SNR (Liu et al. 2019; Qiao et al. 2019; Zhang et al. 2021).

3.3. Spectra and anisotropy of Monogem SNR

Similar to the results of Geminga SNR, the model calculations of Monogem SNR are also presented in Figure 5. The proton spectrum is also consistent with observations. However, the calculated anisotropy greatly overthrows the observations. Obviously, the tension exists between spectrum and anisotropy. In addition, the cut-off energy of electron spectrum is also beyond TeV energy.

It should notice that the spin-down energy of Monogem pulsar is lower than Geminga pulsar with the value ($1.8e^{48}/1.25e^{49}$). It is possible that the injection power of Monogem SNR is much lower than Geminga SNR. In fact, the γ -ray emission at TeV energy is much lower for Monogem to Geminga (Abeysekara et al. 2017). In Figure 5, the dashed line shows the corrected injection energy result by the spin-down energy. Under the circumstances, the contribution from Monogem SNR can be ignored.

Another reason is the propagation effect of source region. It is well known that the propagation coefficient at source region is much lower (Abeysekara et al. 2017). This means that the CRs spend more time to disentangle from the source. The age of Monogem is at the level of 86 kyrs and only limited part of the CRs from Monogem arrive at our solar system.

In a word, the contribution from Monogem SNR is possibly limited. Other information is required to check our model.

3.4. Spectra and anisotropy of Vela SNR

Vela SNR is a very young and nearest celestial body. It will take very important clue to check our model. Figure 6 shows the expected spectrum and anisotropy for electron. The related parameters are shown in Table 3. It is obvious that there exists a bump structure in spectrum and sharp rising in anisotropy above TeV energy. In fact, the bump structure in spectrum has been hinted by HESS, VERTITAS, DAMPE and CALET observations (DAMPE Collaboration et al. 2017; Motz et al. 2021; Archer et al. 2018; Aharonian et al. 2008) as shown in Figure 7. In addition, the electron anisotropy reveals an remarkable hoist, and reach 10% at several TeV. More convincing is that those abnormal phenomena can be tested soon. Firstly, the space-borne experiments DAMPE and HERD will observe the new spectral structure in the short run. Simultaneously, the anisotropy is overwhelming larger for electron than the CRs, which make it easily observed by ground-based experiments HAWC and LHAASO-WCDA.

Considering the importance of Vela SNR, it is necessary to perform further study such as the different ages. Figure 8 shows the spectra and anisotropy at 10, 100, 300 and 500 kyrs for proton and electron. It is obvious that the flux reaches maximum at 100 kyrs and decreases smoothly. When the source age becomes as old as 500 kyrs, the contribution can be ignored. In a word, Vela SNR will play the role of Monogem at ~ 100 kyrs, Geminga at ~ 300 kyrs and disappear above 500 kyrs.

4. CONCLUSION

With new generation of space-borne and ground-based experiments, the measurements of CR spectra and anisotropy step into precise era. Then the fine structure in spectra and anisotropy from TeV to hundreds TeV were observed by those high precision experiments. To reproduce those phenomena, the local source is required for the model calculation. In this work, we systematically study the contribution of all local SNRs within 1 kpc around solar to the spectra of nuclei and electron. Detailed studies show that Geminga, Monogem and Vela SNRs have important contribution to the spectrum of proton and electron. However, the anisotropy of Monogem are obvious tension with observations. In fact, considering the spin-down energy of Monogem pulsar is lower about an order of magnitude than Geminga pulsar, the injection power maybe lower. When we calibrate the total energy of accelerated by this scale, the

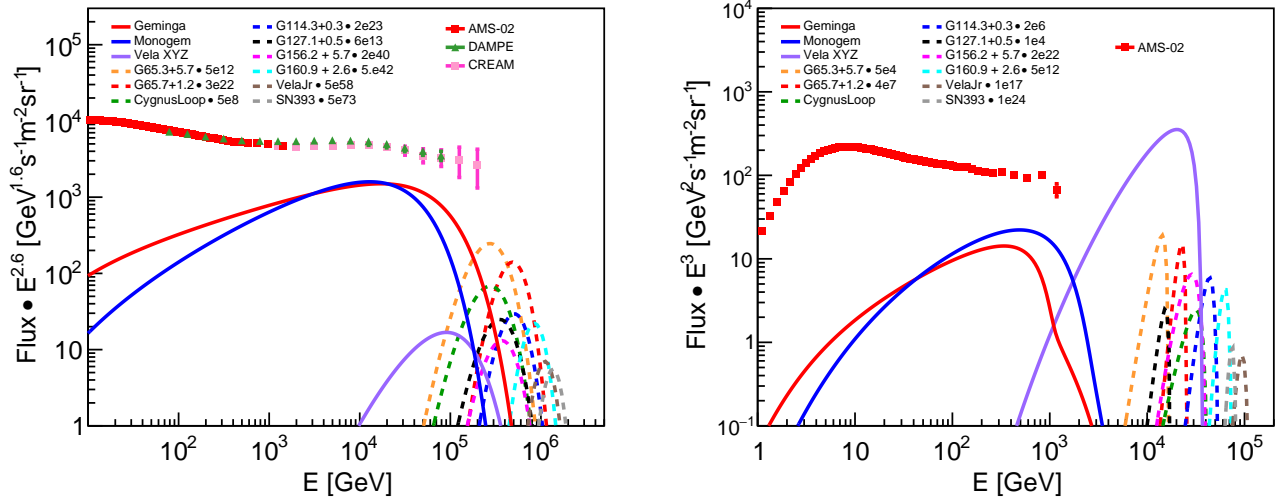


Fig. 3. The computed energy spectra of protons(left) and electrons(right) from the different local SNRs. The red, blue and purple solid lines represent the energy spectral of Geminga, Monogem and Vela SNR. The dashed lines with different colors represent the energy spectra of other local SNRs respectively. For comparing the results conveniently, the fluxes of some local SNRs are multiplied by a scale factor. The red-square, green-triangle and magenta-square data points are from the AMS-02, DAMPE and CREAM experiments respectively(Aguilar et al. 2015b,a; Yoon et al. 2017; An et al. 2019).

Bckgroud	Normalization [†] [(m ² · sr · s · GeV) ⁻¹]	$\nu 1$	\mathcal{R}_{br1}	$\nu 2$	\mathcal{R}_{br2}	$\nu 3$
P Electron	4.62×10^{-2}	2	6	2.41	7×10^6	
	2.80×10^{-1}	1.50	5.10	2.83	300	2.67
SNR	r_{snr} [kpc]	t_{snr} [yrs]	γ_{snr}	\mathcal{R}_c [TV]	q_0^{prot} [GeV ⁻¹]	q_0^{elec} [GeV ⁻¹]
Geminga	0.33	3.45×10^5	2.13	55	2.50×10^{52}	1.20×10^{50}
Monogem	0.29	8.60×10^4	2.13	27	1.20×10^{52}	2.10×10^{49}
Others	$2\alpha_r + 1$	55	2.50×10^{52}	1.20×10^{50}

[†]The proton and electron normalization are set at kinetic energy per nucleon $E_k = 100$ GeV/n and 10 GeV/n respectively.

Tab. 2. The background and local SNRs injected parameters for proton and electron. The age and distance parameters of local sources refer to Table 1.

contribution from Monogem can be neglected. Under such scenario, only Gminga SNR is the dominant source to be responsible for nuclear spectra and anisotropy. More interesting is that the electron spectrum has a new structure above several TeV from the young SNR Vela. Simultaneously, the anisotropy can reach 10% at several TeV energy. Even if the injected energy decreases an order of magnitude, the excesses of spectrum and anisotropy are also obvious. It should be noticed that those excesses can be soon checked by space-borne DAMPE and HERD and ground-based HAWC and LHAASO experiments.

ACKNOWLEDGEMENTS

This work is supported by the National Key R&D Program of China grant No. 2018YFA0404202, the National Natural Science Foundation of China (Nos. 11635011, 11875264, U1831129, U1831208, U2031110).

Note added in proof. While this paper was ready to submit, a similar work appears in <https://arxiv.org/> (Tang et al. 2021).

REFERENCES

Aartsen, M. G., Abbasi, R., Abdou, Y., et al. 2013, ApJ, 765, 55
Aartsen, M. G., Abraham, K., Ackermann, M., et al. 2016, ApJ, 826, 220

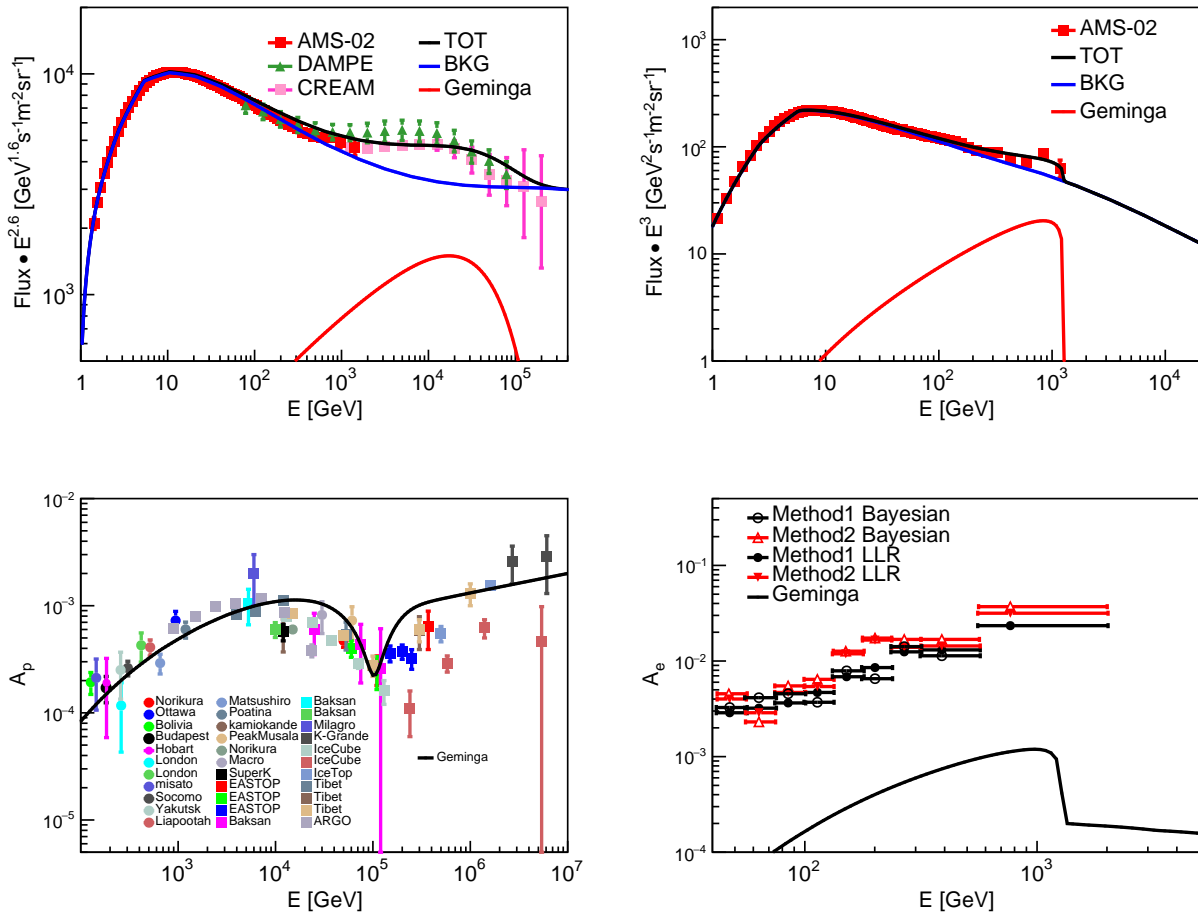


Fig. 4. The computed energy spectral (top) and anisotropy (bottom) for proton (left) and primary electron (right) from Geminga SNR respectively. For energy spectral, the blue lines are the fluxes from the background sources, the red lines are the fluxes from the local Geminga, and the black solid lines are their sum correspondingly. For anisotropies, the black solid lines are the model expected results.

Abbasi, R., Abdou, Y., Abu-Zayyad, T., et al. 2010, ApJ, 718, L194
—. 2011, ApJ, 740, 16
—. 2012, ApJ, 746, 33
Abdo, A. A., Allen, B., Aune, T., et al. 2008, Physical Review Letters, 101, 221101
Abdo, A. A., Allen, B. T., Aune, T., et al. 2009, ApJ, 698, 2121
Abdollahi, S., Ackermann, M., Ajello, M., et al. 2017, Physical Review Letters, 118, 091103
Abeysekara, A. U., Alfaro, R., Alvarez, C., et al. 2014, ApJ, 796, 108
Abeysekara, A. U., Albert, A., Alfaro, R., et al. 2017, Science, 358, 911
Ackermann, M., Ajello, M., Allafort, A., et al. 2013, Science, 339, 807

Adriani, O., Barbarino, G. C., Bazilevskaya, G. A., et al. 2011, Science, 332, 69
Aguilar, M., Aisa, D., Alpat, B., et al. 2015a, Physical Review Letters, 115, 211101
—. 2015b, Physical Review Letters, 114, 171103
Aguilar, M., Ali Cavasonza, L., Alpat, B., et al. 2017, Physical Review Letters, 119, 251101
Aharonian, F., Akhperjanian, A. G., Barres de Almeida, U., et al. 2008, Physical Review Letters, 101, 261104
Ahn, H. S., Allison, P., Bagliesi, M. G., et al. 2010, ApJ, 714, L89
Alemano, F., An, Q., Azzarello, P., et al. 2021, Phys. Rev. Lett., 126, 201102
Alvarez, H., Aparici, J., May, J., & Reich, P. 2001, A&A, 372, 636
Amenomori, M., Ayabe, S., Cui, S. W., et al. 2005, ApJ, 626, L29

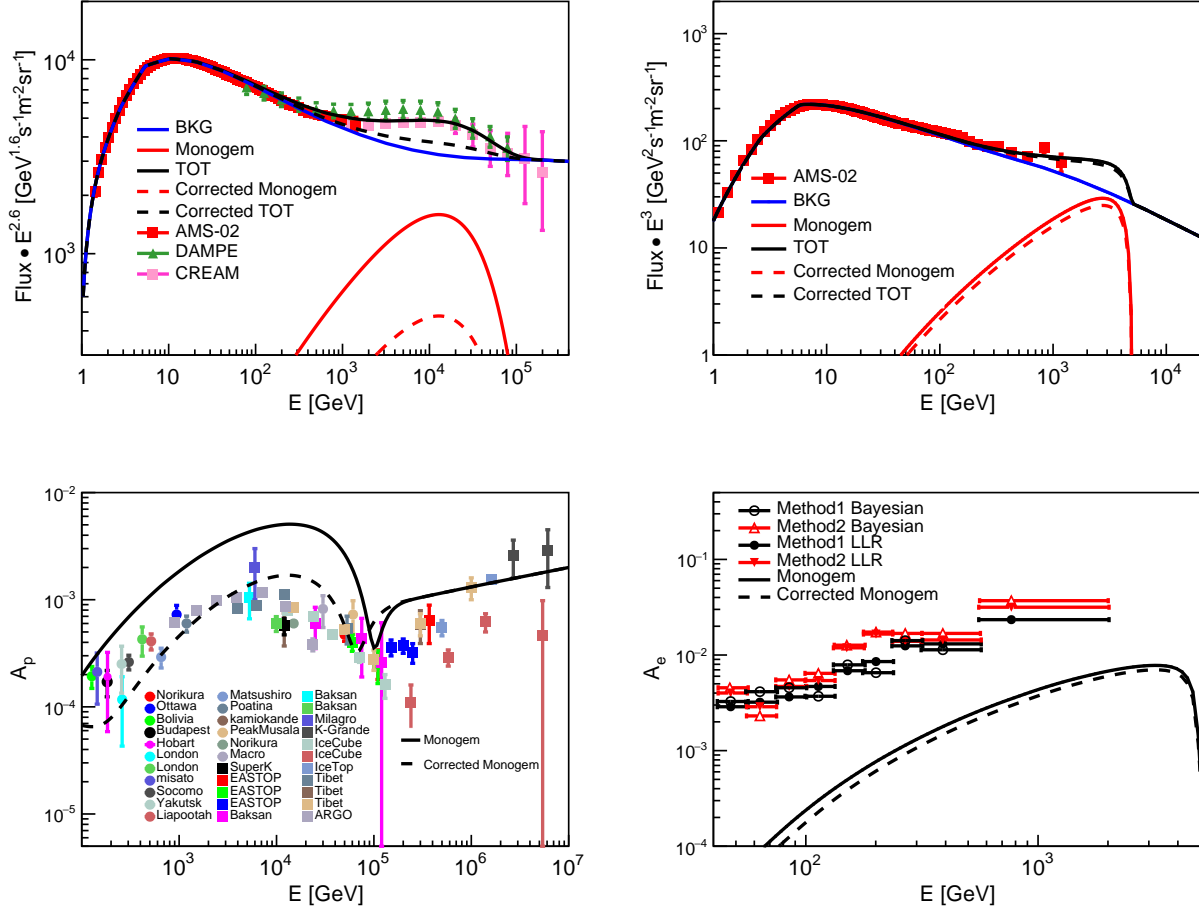


Fig. 5. The computed energy spectral (top) and anisotropy (bottom) for proton (left) and primary electron (right) from Monogem SNR respectively. The implication of different color solid lines is the same as in Figure 4 and the different color dashed lines display the corrected injection energy in accordance with the spin-down energy of Geminga and Monogem pulsars.

Bckgroud (DAMPE)	Normalization [†] $[(m^2 \cdot sr \cdot s \cdot GeV)^{-1}]$	$\nu 1$	\mathcal{R}_{br1} [GV]	$\nu 2$	\mathcal{R}_{br2} [GV]	$\nu 3$
Electron	2.55×10^{-1}	1.60	5.10	2.72	1200	2.80
SNR	r_{snr} [kpc]	t_{snr} [yrs]	γ_{snr}	\mathcal{R}_c [TV]	q_0^{elec} [GeV $^{-1}$]	
Geminga	0.33	3.45×10^5	2.13	55	2.30×10^{50}	
Vela	0.30	1.12×10^4	2.10	55	5.00×10^{49}	

[†]The normalization is set at kinetic energy per nucleon $E_k = 10$ GeV/n.

Tab. 3. Electron background and local SNRs injected parameters about DAMPE experiment.

Amenomori, M., Ayabe, S., Bi, X. J., et al. 2006, Science, 314, 439

Amenomori, M., Bi, X. J., Chen, D., et al. 2010, ApJ, 711, 119

—. 2017, ApJ, 836, 153

An, Q., Asfandiyarov, R., Azzarello, P., et al. 2019, Science Advances, 5, eaax3793

Archer, A., Benbow, W., Bird, R., et al. 2018, Phys. Rev. D, 98, 062004

Aschenbach, B. 1998, Nature, 396, 141

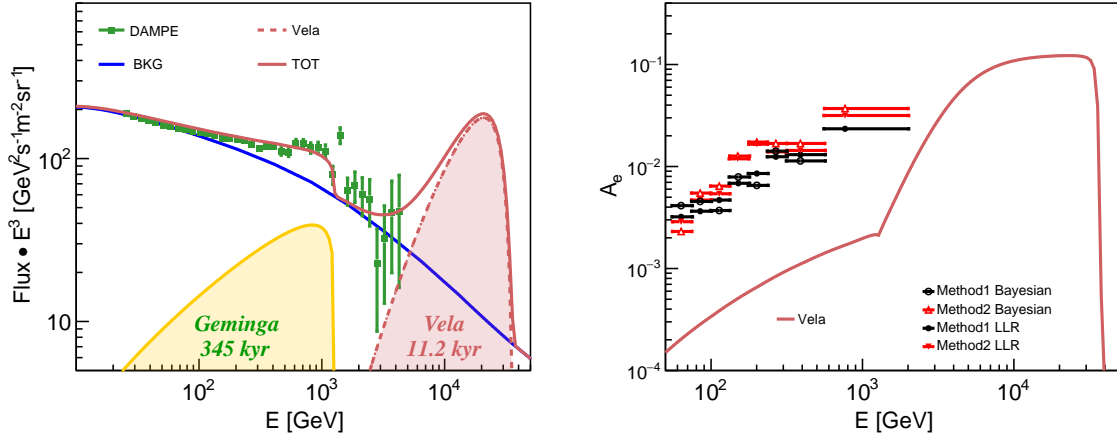


Fig. 6. Left: The calculated total positron and electron spectra of Vela SNR. The blue solid line is the total background flux. The yellow solid line with shadow indicates the Geminga SNR flux. The light-red dashed line with shadow represent the flux from Vela SNR for different injected energy. The corresponding solid line are the sum of background, Geminga and Vela fluxes. The green squares are the measurements from the DAMPE experiment(DAMPE Collaboration et al. 2017). Right: Anisotropies of electron with Geminga and Vela SNR under the SDP model. Both the black and red markers are the upper limits set by the *Fermi*-LAT experiment(Abdollahi et al. 2017).

Atkin, E., Bulatov, V., Dorokhov, V., et al. 2017, *J. Cosmology Astropart. Phys.*, 7, 020

—. 2018, *Soviet Journal of Experimental and Theoretical Physics Letters*, 108, 5

Atoyan, A. M., Aharonian, F. A., & Völk, H. J. 1995, *Phys. Rev. D*, 52, 3265

Bartoli, B., Bernardini, P., Bi, X. J., et al. 2013, *Phys. Rev. D*, 88, 082001

—. 2015, *ApJ*, 809, 90

Bernard, G., Delahaye, T., Salati, P., & Taillet, R. 2012, *A&A*, 544, A92

Blair, W. P., Sankrit, R., & Raymond, J. C. 2005, *AJ*, 129, 2268

Blasi, P. 2013, *A&A Rev.*, 21, 70

Boulares, A. 1989, *ApJ*, 342, 807

Brisken, W. F., Thorsett, S. E., Golden, A., & Goss, W. M. 2003, *ApJ*, 593, L89

Caraveo, P. A., De Luca, A., Mignani, R. P., & Bignami, G. F. 2001, *ApJ*, 561, 930

Cha, A. N., Sembach, K. R., & Danks, A. C. 1999, *ApJ*, 515, L25

DAMPE Collaboration, Ambrosi, G., An, Q., et al. 2017, *Nature*, 552, 63

Di Mauro, M., Donato, F., Fornengo, N., Lineros, R., & Vittino, A. 2014, *J. Cosmology Astropart. Phys.*, 4, 6

Fang, K., Bi, X.-J., & Yin, P.-F. 2018a, *ApJ*, 854, 57

Fang, K., Bi, X.-J., Yin, P.-F., & Yuan, Q. 2018b, *ApJ*, 863, 30

Fang, K., Wang, B.-B., Bi, X.-J., Lin, S.-J., & Yin, P.-F. 2017, *ApJ*, 836, 172

Feng, J., Tomassetti, N., & Oliva, A. 2016, *Phys. Rev. D*, 94, 123007

Gleeson, L. J., & Axford, W. I. 1968, *ApJ*, 154, 1011

Gorham, P. W., Ray, P. S., Anderson, S. B., Kulkarni, S. R., & Prince, T. A. 1996, *ApJ*, 458, 257

Green, D. A. 2014, *Bulletin of the Astronomical Society of India*, 42, 47

—. 2015, *MNRAS*, 454, 1517

Guillian, G., Hosaka, J., Ishihara, K., et al. 2007, *Phys. Rev. D*, 75, 062003

Guo, Y.-Q., Tian, Z., & Jin, C. 2016, *ApJ*, 819, 54

Guo, Y.-Q., & Yuan, Q. 2018, *Phys. Rev. D*, 97, 063008

Iyudin, A. F., Schönfelder, V., Bennett, K., et al. 1998, *Nature*, 396, 142

Jin, C., Guo, Y.-Q., & Hu, H.-B. 2016, *Chinese Physics C*, 40, 015101

Joncas, G., Roger, R. S., & Dewdney, P. E. 1989, *A&A*, 219, 303

Katsuda, S., Petre, R., Hwang, U., et al. 2009, *PASJ*, 61, S155

Katsuda, S., Tsunemi, H., & Mori, K. 2008, *ApJ*, 678, L35

Kothes, R., Fedotov, K., Foster, T. J., & Uyaniker, B. 2006, *A&A*, 457, 1081

Kothes, R., Landecker, T. L., Reich, W., Safi-Harb, S., & Arzoumanian, Z. 2008, *ApJ*, 687, 516

Lazendic, J. S., Slane, P. O., Gaensler, B. M., et al. 2004, *ApJ*, 602, 271

Leahy, D., & Tian, W. 2006, *A&A*, 451, 251

Leahy, D. A., & Tian, W. W. 2007, *A&A*, 461, 1013

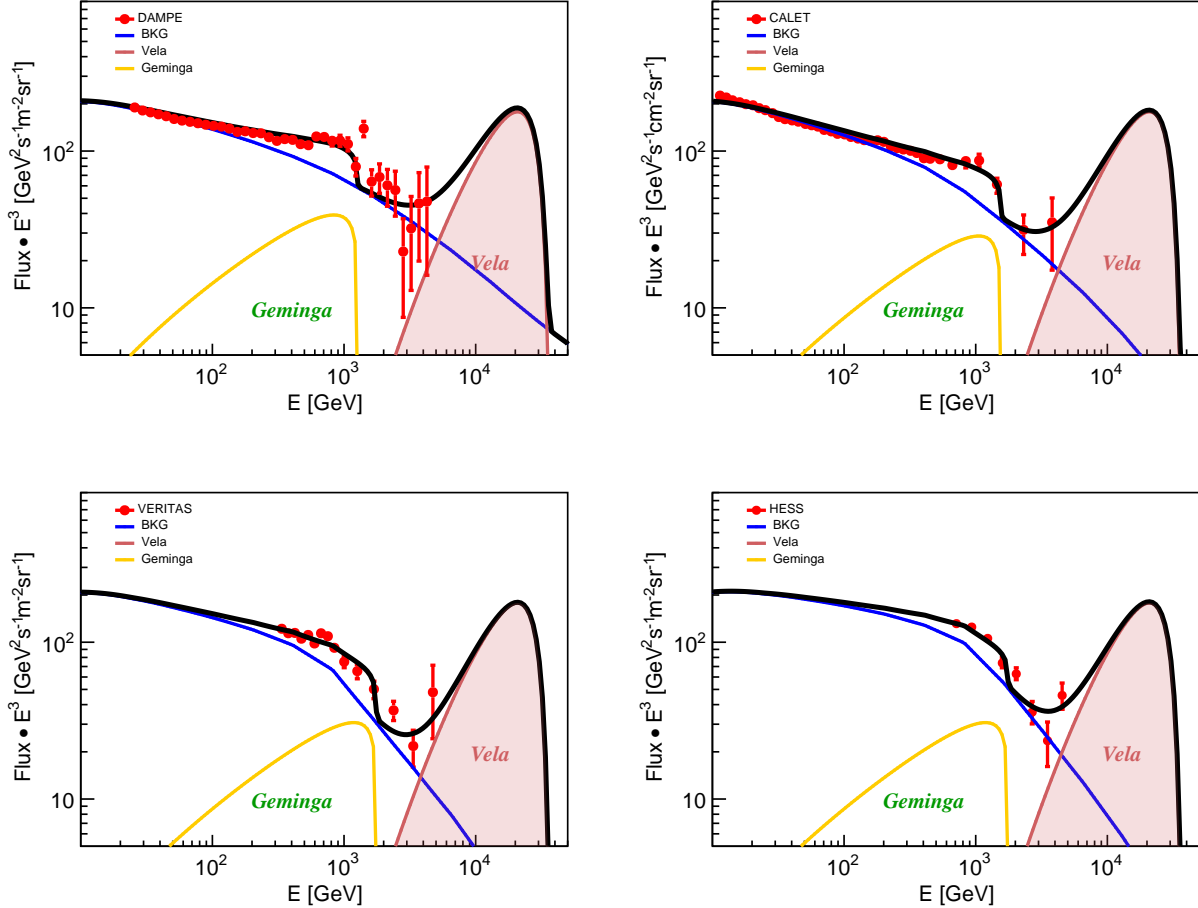


Fig. 7. Model expectations of the electron and positron total spectral compared with the DAMPE(left-top), CALET(right-top), VERITAS(left-bottom) and HESS(right-bottom) experiments respectively. The bule solid lines represent the fluxes from the background sources, the yellow lines are the fluxes of Geminga SNR, the red lines with shadow are the fluxes from Vela SNR and the black lines indicate the sum of the above components.

Liu, W., Bi, X.-J., Lin, S.-J., Wang, B.-B., & Yin, P.-F. 2017, Phys. Rev. D, 96, 023006
 Liu, W., Guo, Y.-Q., & Yuan, Q. 2019, J. Cosmology Astropart. Phys., 2019, 010
 Liu, W., Yao, Y.-h., & Guo, Y.-Q. 2018, ApJ, 869, 176
 Malkov, M. A., & Moskalenko, I. V. 2020, arXiv e-prints, arXiv:2010.02826
 Mavromatakis, F., Boumis, P., Papamastorakis, J., & Ventura, J. 2002, A&A, 388, 355
 Mertsch, P. 2011, J. Cosmology Astropart. Phys., 2, 31
 Miceli, M., Bocchino, F., & Reale, F. 2008, ApJ, 676, 1064
 Morlino, G., Amato, E., & Blasi, P. 2009, MNRAS, 392, 240
 Motz, H., Link, J. T., Adriani, O., Akaike, Y., & De, N. G. A. 2021, in 37th International Cosmic Ray Conference
 Panov, A. D., Adams, J. H., J., Ahn, H. S., et al. 2007, Bulletin of the Russian Academy of Sciences, Physics, 71, 494

Panov, A. D., Adams, J. H., Ahn, H. S., et al. 2009, Bulletin of the Russian Academy of Sciences, Physics, 73, 564
 Perko, J. S. 1987, A&A, 184, 119
 Plucinsky, P. P., Snowden, S. L., Aschenbach, B., et al. 1996, ApJ, 463, 224
 Qiao, B.-Q., Liu, W., Guo, Y.-Q., & Yuan, Q. 2019, J. Cosmology Astropart. Phys., 2019, 007
 Redman, M. P., & Meaburn, J. 2005, MNRAS, 356, 969
 Reich, W., Fuerst, E., & Arnal, E. M. 1992, A&A, 256, 214
 Reich, W., Sun, X. H., Reich, P., et al. 2014, A&A, 561, A55
 Reich, W., Zhang, X., & Fürst, E. 2003, A&A, 408, 961
 Seo, E. S., & Ptuskin, V. S. 1994, ApJ, 431, 705
 Serpico, P. D. 2012, Astroparticle Physics, 39, 2
 Smith, V. V., Cunha, K., & Plez, B. 1994, A&A, 281, L41

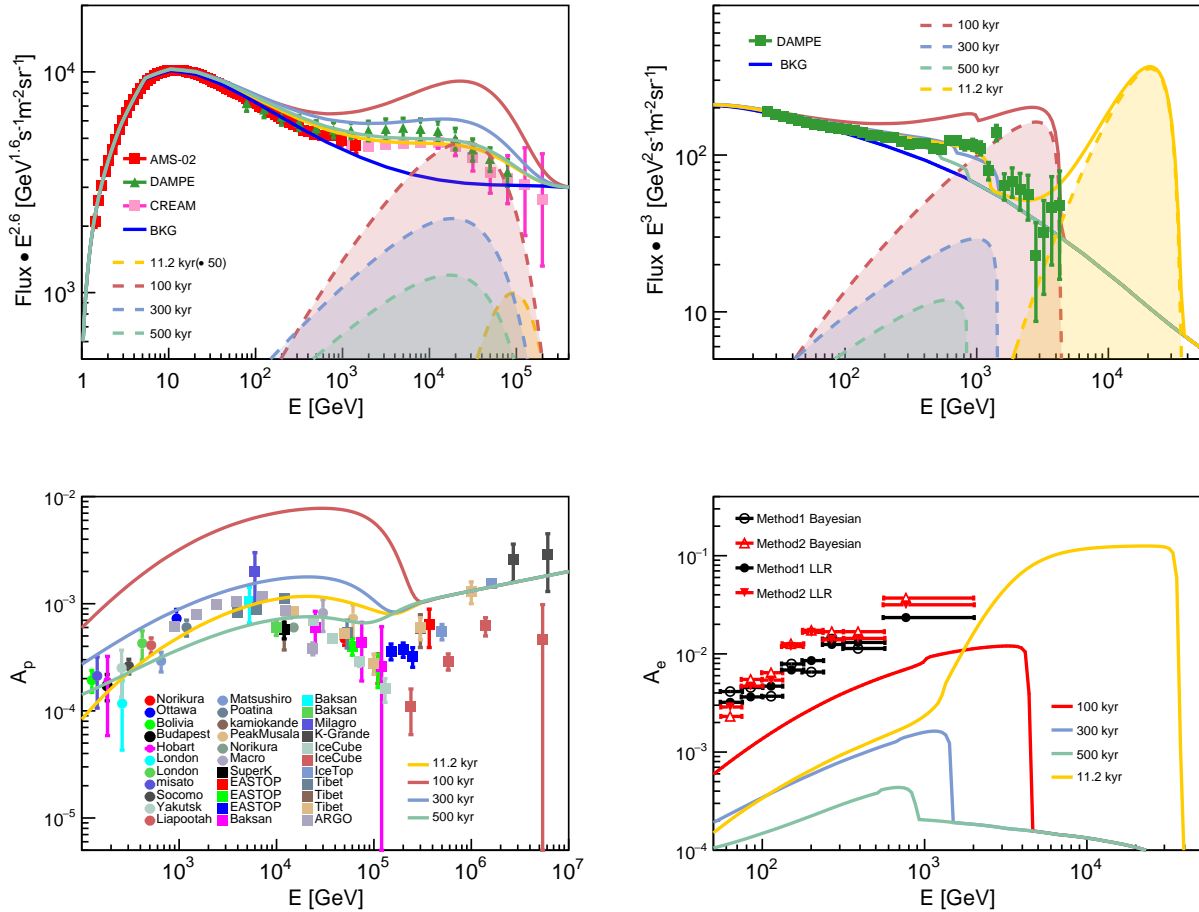


Fig. 8. The computed energy spectral (top) and anisotropy (bottom) for proton (left) and primary electron (right) from Vela SNR respectively. For energy spectral, the blue lines are the fluxes from the background sources, the different color dashed lines are the fluxes from the Vela SNR for various ages, and the different solid lines are their sum including Geminga SNR flux correspondingly. Notice that the Geminga SNR spectrum is not shown here. For anisotropies, the different color solid lines are the model expected results.

Sun, X. H., Reich, W., Han, J. L., Reich, P., & Wielebinski, R. 2006, A&A, 447, 937

Sveshnikova, L. G., Strelnikova, O. N., & Ptuskin, V. S. 2013, Astroparticle Physics, 50, 33

Tang, T.-P., Xia, Z.-Q., Shen, Z.-Q., et al. 2021, Explanation of nearby SNRs for primary electron excess and proton spectral bump, arXiv:2109.12496

Tang, X., & Piran, T. 2019, MNRAS, 484, 3491

Tian, Z., Liu, W., Yang, B., et al. 2020, Chinese Physics C, 44, 085102

Tomassetti, N. 2012, ApJ, 752, L13

—. 2015, Phys. Rev. D, 92, 081301

Vladimirov, A. E., Jóhannesson, G., Moskalenko, I. V., & Porter, T. A. 2012, ApJ, 752, 68

Xiao, L., Reich, W., Fürst, E., & Han, J. L. 2009, A&A, 503, 827

Xu, J. W., Han, J. L., Sun, X. H., et al. 2007, A&A, 470, 969

Yamauchi, S., Yokogawa, J., Tomida, H., Koyama, K., & Tamura, K. 2000, in Broad Band X-ray Spectra of Cosmic Sources, ed. K. Makishima, L. Piro, & T. Takahashi, 567

Yar-Uyaniker, A., Uyaniker, B., & Kothes, R. 2004, ApJ, 616, 247

Yoon, Y. S., Anderson, T., Barrau, A., et al. 2017, ApJ, 839, 5

Yuan, Q., & Bi, X.-J. 2013, Physics Letters B, 727, 1

Yuan, Q., & Feng, L. 2018, Science China Physics, Mechanics, and Astronomy, 61, 101002

Yuan, Q., Qiao, B.-Q., Guo, Y.-Q., Fan, Y.-Z., & Bi, X.-J. 2020, arXiv e-prints, arXiv:2007.01768

Zhang, P.-p., Qiao, B.-q., Liu, W., et al. 2021, J. Cosmology Astropart. Phys., 2021, 012